Tumor MHC Class I Expression Associates with Intralesional IL2 Response in Melanoma

Maryam Pourmaleki[1,2], Caitlin J. Jones[3], Charlotte E. Ariyan[4], Zheng Zeng[3], Mono Pirun[3], Daniel A. Navarrete[1], Yanyun Li[5], Mianlei Zhang[5], Subhiksha Nandakumar[6], Carl Campos[1], Saad Nadeem[7], David S. Klimstra[5], Claire F. Temple-Oberle[8,9], Thomas Brenn[10], Evan J. Lipson[11], Kara M. Schenk[11], Julie E. Stein[12], Janis M. Taube[11,12,13], Michael G. White[14], Raymond Traweek[14], Jennifer A. Wargo[14,15], John M. Kirkwood[16], Billel Gasmi[17,18], Stephanie L. Goff[17], Alex D. Corwin[19], Elizabeth McDonough[19], Fiona Ginty[19], Margaret K. Callahan[20,21,22], Andrea Schietinger[23,24], Nicholas D. Socci[3,6], Ingo K. Mellinghoff[1,25,26], and Travis J. Hollmann[5,22]

ABSTRACT

Cancer immunotherapy can result in lasting tumor regression, but predictive biomarkers of treatment response remain ill-defined. Here, we performed single-cell proteomics, transcriptomics, and genomics on matched untreated and IL2 injected metastases from patients with melanoma. Lesions that completely regressed following intralesional IL2 harbored increased fractions and densities of nonproliferating $CD8^+$ T cells lacking expression of PD-1, LAG-3, and TIM-3 ($PD\text{-}1^-LAG\text{-}3^-TIM\text{-}3^-$). Untreated lesions from patients who subsequently responded with complete eradication of all tumor cells in all injected lesions (individuals referred to herein as "extreme responders") were characterized by proliferating $CD8^+$ T cells with an exhausted phenotype ($PD\text{-}1^+LAG\text{-}3^+TIM\text{-}3^+$), stromal B-cell aggregates, and expression of IFNγ and IL2 response genes. Loss of membranous MHC class I expression in tumor cells of untreated lesions was associated with resistance to IL2 therapy. We validated this finding in an independent cohort of metastatic melanoma patients treated with intralesional or systemic IL2. Our study suggests that intact tumor-cell antigen presentation is required for melanoma response to IL2 and describes a multidimensional and spatial approach to develop immuno-oncology biomarker hypotheses using routinely collected clinical biospecimens.

Introduction

Up to 20% of patients with metastatic cutaneous melanoma present with "in-transit" metastasis, a form of locoregional recurrence (1). Therapeutic options for in-transit melanoma include surgical excision, isolated limb perfusion, radiation, systemic therapies, and intralesional therapies, including IL2, which was the first FDA-approved immunotherapeutic agent (2, 3). Today, IL2 is regaining popularity as an immuno-oncology agent as a number of pharmaceutical companies have IL2 candidates in clinical trials for a variety of solid cancers (4). Compared with systemic IL2 administration, intralesional IL2 injection reduces systemic toxicity while maximizing intratumoral IL2 concentration. Prior studies have reported that 41%–96% of injected lesions show a complete response (CR) to IL2 (3, 5). Although responding lesions have been shown to harbor increased densities of $CD8^+$ T cells (6, 7), more detailed molecular and cellular effects of

[1]Human Oncology and Pathogenesis Program, Memorial Sloan Kettering Cancer Center, New York, New York. [2]Tri-Institutional Program in Computational Biology and Medicine, Weill Cornell School of Medicine, New York, New York. [3]Bioinformatics Core, Memorial Sloan Kettering Cancer Center, New York, New York. [4]Department of Surgery, Memorial Sloan Kettering Cancer Center, New York, New York. [5]Department of Pathology, Memorial Sloan Kettering Cancer Center, New York, New York. [6]Marie-Josée and Henry R. Kravis Center for Molecular Oncology, Memorial Sloan Kettering Cancer Center, New York, New York. [7]Department of Medical Physics, Memorial Sloan Kettering Cancer Center, New York, New York. [8]Department of Surgery, University of Calgary, Calgary, Alberta, Canada. [9]Department of Oncology, University of Calgary, Calgary, Alberta, Canada. [10]Department of Pathology, University of Calgary, Calgary, Alberta, Canada. [11]Department of Oncology, The Johns Hopkins University School of Medicine, The Sidney Kimmel Comprehensive Cancer Center, and The Johns Hopkins Bloomberg-Kimmel Institute for Cancer Immunotherapy, Baltimore, Maryland. [12]Department of Pathology, The Johns Hopkins University School of Medicine, The Sidney Kimmel Comprehensive Cancer Center, and The Johns Hopkins Bloomberg-Kimmel Institute for Cancer Immunotherapy, Baltimore, Maryland. [13]Department of Dermatology, The Johns Hopkins University School of Medicine, The Sidney Kimmel Comprehensive Cancer Center, and The Johns Hopkins Bloomberg-Kimmel Institute for Cancer Immunotherapy, Baltimore, Maryland. [14]Department of Surgical Oncology, The University of Texas MD Anderson Cancer Center, Houston, Texas. [15]Department of Genomic Medicine, The University of Texas MD Anderson Cancer Center, Houston, Texas. [16]Department of Medicine, University of Pittsburgh, Pittsburgh, Pennsylvania. [17]Surgery Branch, National Cancer Institute, National Institutes of Health, Bethesda, Maryland. [18]Laboratory of Pathology, National Cancer Institute, National Institutes of Health, Bethesda, Maryland. [19]Biology and Applied Physics, GE Global Research Center, Niskayuna, New York. [20]Department of Medicine, Memorial Sloan Kettering Cancer Center, New York, New York. [21]Weill Cornell Medical College, New York, New York. [22]Parker Institute for Cancer Immunotherapy, San Francisco, California. [23]Immunology Program, Sloan Kettering Institute, Memorial Sloan Kettering Cancer Center, New York, New York. [24]Immunology and Microbial Pathogenesis Program, Weill Cornell School of Medicine, New York, New York. [25]Department of Neurology, Memorial Sloan Kettering Cancer Center, New York, New York. [26]Department of Pharmacology, Weill Cornell School of Medicine, New York, New York.

Note: Supplementary data for this article are available at Cancer Immunology Research Online (http://cancerimmunolres.aacrjournals.org/).

Corresponding Authors: Ingo K. Mellinghoff, Department of Neurology, Memorial Sloan Kettering Cancer Center, 1275 York Avenue, New York, NY 10065. Phone: 646-888-2766; E-mail: mellingi@mskcc.org; and Travis J. Hollmann, Phone: 212-639-8134; E-mail: hollmant@mskcc.org

Cancer Immunol Res 2022;10:303–13

doi: 10.1158/2326-6066.CIR-21-1083

intralesional IL2 and biomarkers of response are unknown. In this study, we used single-cell proteomics and bulk transcriptomics and genomics to identify changes in the tumor microenvironment and biomarkers of response associated with intralesional IL2 therapy for patients with melanoma while describing a multidimensional approach for biomarker hypothesis development.

Materials and Methods

Patients and tissue

This study includes all patients with in-transit melanoma who presented for intralesional IL2 therapy at Memorial Sloan Kettering Cancer Center (MSKCC) from 2015 to 2017 ($n = 7$) and who met the criteria of having untreated and IL2-injected tissue and subsequent IL2-response data at the level of each injected lesion (Supplementary Table S1). All patients signed statements of informed consent under protocols approved by the MSKCC Institutional Review Board, and the study was conducted in accordance with the Declaration of Helsinki. All lesions were surgically resected (Charlotte E. Ariyan) and immediately formalin-fixed and paraffin-embedded (FFPE). All biospecimens were obtained as part of routine clinical care with standard FFPE tissue processing in the MSKCC surgical pathology lab (CLIA accredited). FFPE tissue blocks were maintained in the MSKCC Department of Pathology temperature controlled storage units until use. For each specimen, adjacent tissue sections were freshly cut for hematoxylin and eosin (H&E; 1 section, 5 μm), multiplexed immunofluorescence (multiplexed IF; Cell Dive, Cytvia; 1 section, 5 μm), NanoString (10 sections, 10 μm), MSK-IMPACT (20 sections, 5 μm), and immunohistochemistry (IHC) for MHC class I (1 section, 4 μm). Cell Dive validation IHCs were completed on 28 additional 4-μm thick tissue sections from lesion 3_2. Multiplexed IF (tyramide-based assay) was completed on one 4-μm thick tissue section. H&Es were reviewed by a board-certified dermatopathologist (Travis J. Hollmann) for classification of treatment response as either CR or non-CR based on the presence or absence of tumor cells, respectively.

Our validation cohort includes 19 patients with metastatic melanoma who received intralesional IL2 or high-dose systemic IL2 and who met the criteria of having untreated tissue with no prior therapies and subsequent IL2-response data at the level of each injected lesion for intralesional IL2 therapy and at the level of the patient for high-dose systemic IL2 therapy. All patients signed statements of informed consent, and the study was conducted in accordance with the Declaration of Helsinki. All lesions were surgically resected and immediately submitted for standard FFPE tissue processing. "CR" denotes full regression of the tumor following IL2 therapy, whereas "non-CR" denotes remaining tumor cells following IL2 therapy.

Targeted RNA sequencing using NanoString

NanoString was performed for all lesions in the initial discovery cohort with the exception of lesions 3_2 and 6_2, which were excluded due to low RNA quantity post-extraction. RNA extraction was performed after macrodissection to exclude necrotic and normal skin regions. FFPE sections were deparaffinized using the mineral oil method. Briefly, 800 μL mineral oil (Thermo Fisher cat. #AC415080010) was mixed with the sections, and the sample was incubated at 65°C for 10 minutes. Phases were separated by centrifugation in 360 μL Buffer PKD (DNeasy Blood and Tissue Kit, QIAGEN cat. #69504), and Proteinase K (600 mAU/mL; DNeasy Blood and Tissue Kit, QIAGEN cat. #69504) was added for digestion. After a three-step incubation (65°C for 45′, 80°C for 15′, and 65°C for 30′) and additional centrifugation, the aqueous phase containing RNA was removed and DNase treated (DNeasy Blood and Tissue Kit, QIAGEN cat. #69504). The RNA was then extracted using the RNeasy FFPE Kit (QIAGEN cat. #73504) according to the manufacturer's instructions. A minimum of 100 ng of total RNA per sample was used to measure the expression of 770 immune-related genes and 20 internal reference genes (PanCancer IO 360 gene-expression panel) using NanoString Technologies' nCounter platform. Normalization using the internal reference genes was performed using nSolver. Differential expression analysis was run using the DESeq2 Bioconductor package.

Targeted DNA sequencing using MSK-IMPACT

MSK-IMPACT was performed for all tumor-containing untreated and non-CR lesions in the initial discovery cohort with the exception of patient 6 due to tissue availability. DNA extraction was performed after macrodissection to exclude necrotic and normal skin regions. FFPE tissue was deparaffinized using heat treatment (90°C for 10′ in 480 μL PBS and 20 μL 10% Tween 20), centrifugation (10,000 × g for 15′), and ice chill. Paraffin and supernatant were removed, and the pellet was washed with 1 mL of 100% ethanol followed by an incubation overnight in 400 μL of 1 mol/L NaSCN for rehydration and impurity removal. Tissues were subsequently digested with 40 μL of Proteinase K (600 mAU/mL) in 360 μL Buffer ATL (DNeasy Blood and Tissue Kit, QIAGEN, cat. #69504) at 55°C. DNA isolation proceeded with the DNeasy Blood and Tissue Kit (QIAGEN, cat. #69504) according to the manufacturer's protocol modified by replacing buffer AW2 with 80% ethanol. DNA was eluted in 0.5X Buffer AE heated to 55°C. Next-generation sequencing of patient-matched tumor/normal DNA was performed in the MSKCC Integrated Genomics Operation core facility using MSK-IMPACT 468, which has been previously described (8). A genetically matched normal was used for all cases. The current analysis framework can be found at https://github.com/mskcc/roslin-variant/wiki/Roslin-Output-v2.5.

H&E staining

H&E staining was performed for all lesions (initial discovery and validation cohorts) using the Ventana Symphony automated H&E stainer with standard clinical protocol. Tissue sections were baked for one hour at 60°C, hydrated, stained with hematoxylin (Leica, cat. #3801560), stained with bluing reagent (Leica, cat. #3802918), stained with eosin counterstain (Leica, cat. #3801600), rinsed, dehydrated, and coverslipped.

Multiplexed IF staining (Cell Dive)

Multiplexed IF (Cell Dive) was performed for all lesions in the initial discovery cohort. Multiple primary antibody clones were evaluated for each antigen by IHC on normal human multitissue controls (tonsil, placenta, skin, colon, kidney, pancreas, testicle, lung, and spleen; Supplementary Fig. S1; Supplementary Table S2). The normal human controls were processed with standard FFPE tissue processing in the MSKCC surgical pathology lab (CLIA accredited), and FFPE tissue blocks were maintained in the MSKCC Department of Pathology temperature-controlled storage units until use. The most optimal clone was conjugated to Cy2, Cy3, or Cy5 Bis NHS Ester dyes (GE, cat. #PA22000, PA13000, and PA25000, respectively) using a previously published protocol (9). Each conjugated primary antibody was evaluated at three different dilutions to the unconjugated antibody. The staining protocol consists of incubating slides for 60 minutes with the conjugated primary antibody and a 3% BSA in PBS diluent at room temperature followed by three rounds of five-minute washes in 1× PBS. Each epitope was tested for stability to alkaline H_2O_2-based signal inactivation by

exposing adjacent sections of a multitissue control to 0, 1, 5, and 10 cycles of alkaline H_2O_2 followed by staining with the antibody (9).

The multitissue control was included on each slide for quality control. Tissue sections were baked for one hour at 60°C, deparaffinized, hydrated, processed through a two-step antigen retrieval process (step 1: citrate-based pH 6.0, Vector, cat. #H-3300; step 2: EDTA-based pH 8.5, Sigma, cat. #T6066-100G/Bio-Rad, cat. # 161-0729/Sigma, cat. #P9416) using a previously published protocol (9), and blocked overnight using normal donkey serum (Jackson ImmunoResearch, cat. #017-000-121). The tissue was then stained with DAPI for 15 minutes (Thermo Scientific, cat. #D3571) and washed three rounds for five minutes with 1× PBS. A whole slide image was acquired for field-of-view (FOV) selection. FOVs were placed on the tumor–stroma interface, tumor center, and regressed tumor. Tissue sections then underwent 16 cycles of background imaging, staining, imaging, and signal inactivation. Images were acquired using the Cytell Cell Imaging System (Cytvia). Image App software was used for image acquisition and registration (using DAPI), and this functionality is fully incorporated into the commercial Cell Dive product (Leica Microsystems). An acquired background image following each cycle of dye inactivation was used to subtract autofluorescence from the subsequent stain round resulting in autofluorescence removed images.

Multiplexed IF staining (tyramide-based assay)

Multiplexed IF (tyramide-based assay) was performed for all lesions in the initial discovery cohort. Tissue sections were processed using the protocol described for IHC through antigen retrieval followed by three sequential cycles of staining (CD4: 0.7 μg/mL, CD8: 0.125 μg/mL, TIM-3: 0.15 μg/mL) with each round including a 30-minute combined block and primary antibody incubation (Akoya Opal antibody diluent/block cat. #ARD1001). The CD4, CD8, and TIM-3 antibodies used can be found in Supplementary Table S2. CD4 and CD8 detection was performed using 10-minute incubation with a goat anti-mouse poly HRP secondary antibody (Invitrogen, cat. #B40961). The HRP-conjugated secondary antibody polymer was detected using fluorescent tyramide signal amplification using Opal dyes 520 (CD4), 570 (CD8), 650 (TIM-3; Akoya, cat. #FP1487001KT, cat. #FP1488001KT, and cat. #FP1496001KT, respectively). The covalent tyramide reaction was followed by heat-induced stripping of the primary/secondary antibody complex using Akoya AR9 buffer (cat. #AR900250ML) and Leica Bond ER2 (90% ER2 and 10% AR9) at 100°C for 20 minutes preceding the next cycle. After three sequential rounds of staining, sections were stained with Hoechst (Invitrogen, cat. #33342) and mounted with ProLong Gold antifade reagent mounting medium (Invitrogen, cat. #P36930). Whole slide images were acquired using Zeiss AXIO scanner. Indica Labs' HALO Image Analysis software was used for image analysis. Necrotic regions were excluded.

IHC staining

IHC for MHC class I was performed for all lesions (initial discovery and validation cohorts) and for the 28 markers in the multiplexed IF panel (Supplementary Table S2) for lesion 3_2 using an automated staining system (Leica Bond RX) with 3,3′ diaminobenzidine detection (Leica Bond Polymer Refine Detection, cat. #DS9800). Tissue sections were baked for three hours at 62°C in vertical slide orientation with subsequent deparaffinization performed on the Leica Bond RX. Antigen retrieval was conducted for 30 minutes using Leica Bond epitope retrieval solution 2 (ER2; EDTA, pH 9.0; cat. #AR9640) followed by incubation of the primary antibody at previously optimized concentrations for 30 minutes (a list of the primary antibodies used can be found in Supplementary Table S2) followed by incubation of the secondary antibody (Leica Bond Polymer Refine Detection cat. #DS9800). MHC class I staining was scored for the percentage of membrane-positive tumor cells within the entire tissue section in 5% increments (0%–100%). Slides were scored blindly by Travis J. Hollmann and Maryam Pourmaleki. IHC staining for the 28 markers for lesion 3_2 was visually inspected alongside the multiplexed IF (Cell Dive) staining for the 28 markers for lesion 3_2 by Travis J. Hollmann and Maryam Pourmaleki to ensure accuracy of the multiplexed IF method.

Multiplexed IF data analysis (Cell Dive)

Image analysis

HALO was used for image visualization and analysis. For each FOV, images for the 28 markers and DAPI were stacked. Markers with technical issues or nonspecific staining in either a single FOV or the lesion were excluded. High-intensity artifacts were annotated for exclusion. The tumor–stroma interface was manually annotated for each interface FOV using the marker SOX-10, which labels the nuclei of tumor cells. Annotation coordinates were exported for downstream analysis. Nuclear segmentation parameters and thresholds were set for each lesion and optimized using 2 FOVs.

Cell loss computation

DAPI images (first and last cycles, 1 and 32) were processed with intensity normalization and histogram matching. Sum of squared differences was used to generate a pixel level bit mask image highlighting areas of cell loss/drift between images. The bit mask and cell coordinates were used to calculate a loss/drift percentage for each cell.

Data processing

Each cell was assigned a unique ID. Cells in regions with artifacts, in the 20-μm border region of each FOV, and with greater than 10% loss/drift of pixels were removed from analysis. For each interface FOV, we created a quad tree consisting of pixel coordinates of the annotated tumor interface using R-package SearchTrees v0.5.2. For each cell, we identified the nearest point on the tumor interface using k-nearest neighbor lookup on the tree and measured the distance from the cell to that point (0.293 μm per pixel conversion). Each cell falling within ±360 μm of the tumor interface was assigned to a 10-micron interval. Distance in micrometers between all unique pairs of cells in each FOV was calculated for cell neighborhood analyses. Intensity values for each marker were normalized by dividing the intensities for each marker by the value of the threshold. Intensity values below the threshold (less than 1) were flattened to 1. The log of the intensity values for each marker was divided by the width of the log intensity (97.5-percentile value) distribution across the FOV. Cells were assigned to a cell type using positive and negative combinations of cell identity markers. A method was created to reset problematic thresholds.

t-SNE analysis

We performed dimensionality reduction on the full set of marker intensities using the Rtsne package. The normalized/transformed intensities were projected onto two dimensions using the *t*-SNE method with a perplexity of 250 and 5,000 iterations.

Statistical analysis

We transformed fractions to log odds and used R function wilcox.test with the default two-sided option to compute significance of the differences and effect sizes as log odds ratios (OR). We used the same method for log-transformed densities, reporting effect sizes as fold changes. *P* values were adjusted for multiple testing with Bonferroni adjustment.

Statistical integration of overall and intrapatient analyses

From filtered cell fractions for overall CR versus untreated and overall non-CR versus untreated comparisons, we filtered cell fractions with at least one significant overall OR (P-adjusted < 0.05). Harmonic mean P value was calculated for each intrapatient comparison and adjusted using Bonferroni test. The union of untreated lesion FOVs was used for patients with two untreated lesions (#4 and #6).

Tumor MHC class I neighborhoods

Immune cells were grouped by being in MHC I–low, MHC I–mixed, MHC I–high, tumor-free, and isolated neighborhoods (30-μm radius) based on neighborhoods having a maximum of 25% MHC I^+ tumor cells, between 25% and 75% MHC I^+ tumor cells, a minimum of 75% MHC I^+ tumor cells, no tumor cells, or no neighbors, respectively.

Identification of B-cell aggregates

Clusters of B cells were identified using the set of B-cell pairs with less than 30 μm between them. Starting with one pair as a cluster, all B-cell neighbors of both cells in the pair were added to the cluster, followed by neighbors of neighbors. Clusters of 20 B cells or more were labeled B-cell aggregates.

$CD8^+$ T-cell neighborhoods

Immune cells were grouped by being in $CD8^+$ T-cell triple-negative (TN), single-positive (SP), double-positive (DP), or triple-positive (TP) neighborhoods using PD-1, LAG-3, and TIM-3 based on neighborhoods having exclusively one degree of $CD8^+$ T-cell exhaustion (TN, SP, DP, or TP). All other immune cells were excluded from the analysis. Log OR of each cell fraction in groups SP, DP, TP versus TN was computed. Cell fractions were tested for monotonicity as exhaustion progresses using R-package Kendall.

Data and materials availability

All data supporting findings of this study are available online at https://zenodo.org/record/4300912#.YcUQgH3MLFR. All codes and detailed computational methods for multiplexed IF and NanoString analyses are available at https://github.com/mskcc/Halo_Melanoma_IL2.

Results

We identified seven patients with multiple contemporaneous in-transit melanoma metastases, of which at least one metastasis was surgically removed without prior IL2 injection (termed untreated) and at least one metastasis had received IL2 injections prior to resection (**Fig. 1A**). This cohort of matched untreated and IL2-injected lesions provided an opportunity to investigate pretreatment molecular and cellular makeup as well as IL2-associated changes within the tumor that are associated with tumor response to therapy. For each lesion, we assessed the coexpression of 28 proteins at single-cell resolution using multiplexed IF (9, 10), the abundance of 770 immune response–related transcripts (bulk RNA), and the presence or absence of genetic alterations in 468 cancer genes (bulk DNA) in immediately adjacent FFPE tissue sections (**Fig. 1B**).

In total, 9 of 18 (50%) IL2-injected lesions responded completely to intralesional IL2 (termed CR), defined by the absence of tumor cells on histopathologic review. The other 9 of 18 IL2-injected lesions contained abundant residual tumor cells (termed non-CR; **Fig. 1C**; Supplementary Table S1). Two patients (termed extreme responders) experienced complete regression of all IL2-injected lesions, whereas all other patients (termed non-/mixed responders) had at least one IL2-resistant lesion. Metastases from a given patient harbored similar mutations and copy-number profiles (Supplementary Fig. S2A and S2B), supporting their origin from the same primary tumor clone. When compared with a larger cohort of cutaneous melanomas that were sequenced using MSK-IMPACT (8), our cohort showed a similar distribution of genetic alterations (Supplementary Fig. S2B and S2C).

Our selection of markers for single-cell proteomic analysis included markers for both cell identity (e.g., tumor cell) and cell function (e.g., antigen presentation; Supplementary Fig. S1A; Supplementary Table S2). For each marker, we evaluated specificity and sensitivity of the fluorescent dye–conjugated antibody through staining of normal

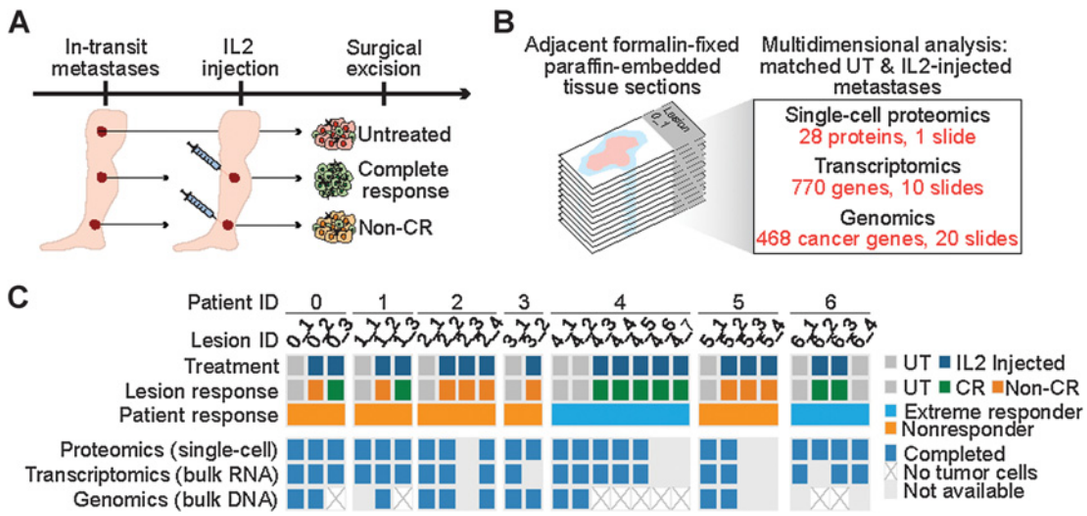

Figure 1.

Multidimensional assessment of in-transit melanoma metastases treated with intralesional IL2. **A,** Study design. Multiple cutaneous in-transit metastases were excised from each melanoma patient, including at least one untreated (UT) and one IL2-injected lesion. Treatment response for IL2-injected lesions was classified as complete response or non-CR. **B,** Allocation of consecutive tumor tissue sections for molecular analyses. **C,** Summary of molecular analyses completed for each lesion. "Nonresponder" refers to all non-/mixed responder patients.

human tissues (Supplementary Fig. S1B and S1C), epitope stability to H_2O_2-based signal inactivation through repeated dye inactivation cycles (Supplementary Fig. S1D), and multiplexed IF staining specificity through staining of adjacent tumor sections with standard IHC (Supplementary Fig. S1E). Using combinations of positivity and negativity for cell identity markers, we defined 16 immune-cell types, tumor cells, adipocyte/Langerhans cells, epithelial cells, and nerve cells (Supplementary Table S3).

To identify functionally distinct subpopulations of tumor and immune cells, we annotated each cell type with combinations of 15 cell-function markers, ultimately resulting in 664 distinct "cell states." For comparisons between samples, the relative abundance of these subpopulations was expressed as cell fractions (e.g., fraction of $Ki67^+$ $CD8^+$ T cells over all $CD8^+$ T cells) and cell densities (e.g., $Ki67^+$ $CD8^+$ T cells per millimeter squared), ultimately amounting to 685 distinct cell fractions and 664 distinct cell densities (Supplementary Fig. S3; Supplementary Table S4).

Following cell segmentation, marker thresholding, and removal of cells displaced during any staining cycle, we identified a total of 2,572,629 cells within 333 high-dimensional FOVs from 22 excised lesions in total (untreated, CR, and non-CR), of which 928,592 were immune cells (Supplementary Fig. S3B; Supplementary Table S5). Examination of multiple FOVs from each lesion allowed us to survey a much broader tumor area than typically examined using tissue microarrays (Supplementary Fig. S4A and S4B; Supplementary Table S5). We observed considerable heterogeneity in the composition of immune-cell infiltrates within FOVs from the same lesion (Supplementary Fig. S4C). At the single-cell level, the expression of some markers appeared mostly restricted to specific immune-cell types (e.g., expression of the IL2 receptor alpha chain CD25 in $CD4^+$ regulatory T cells), whereas other markers (e.g., Ki67) were expressed in all immune-cell types (Supplementary Fig. S3C). Within cell types, certain cell-function markers were more broadly expressed than others (e.g., expression of TIM-3 and CD27 in T cells and B cells; Supplementary Fig. S3D–S3G).

To gain insight into the molecular processes that are associated with a complete lesion response to intralesional IL2, we determined the frequency of each cell state in untreated and IL2-injected lesions (**Fig. 2A**; Supplementary Table S6). Compared with untreated lesions, CR lesions showed increased fractions of $CD8^+$ T cells over all T-cell subtypes and all immune cells, a well-documented effect of IL2 (6, 7). CR lesions also showed increased fractions of PD-1^-LAG-3^-TIM-3^- $CD8^+$ T cells, $CD4^+$ (helper) T cells, $CD4^+$ regulatory T cells, B cells, and natural killer (NK) cells (**Fig. 2A**; Supplementary Fig. S5). CR lesions also showed the lowest fractions of TIM-3^+ cells (across most immune-cell types), a finding that we validated using an independent multiplexed IF platform (**Fig. 2A**; Supplementary Fig. S6A and S6B). This is reminiscent of the reported association between TIM-3 and treatment resistance in other immuno-oncology contexts (11, 12). Non-CR lesions, on the other hand, showed an admixture of immune and tumor cells and no statistically significant change in $CD8^+$ T-cell infiltration compared with untreated lesions (**Fig. 2A**). Interestingly, non-CR lesions did harbor increased numbers of $CD25^+$ $CD4^+$ regulatory T cells, suggesting that failure to upregulate the IL2 receptor alpha (CD25), a well-documented effect of IL2 (13), is not the cause of IL2 resistance in these lesions. We observed no differences in immune-cell populations between multiple untreated lesions from the same patient (Supplementary Fig. S7A and 7B; Supplementary Table S7). Overall, there was considerable heterogeneity in the IL2 response between patients (Supplementary Fig. S8; Supplementary Table S6). For example, non-CR lesions from two patients showed significantly increased fractions of PD-1^-LAG-3^-TIM-3^- $CD8^+$ T cells. However, at the level of the cohort, this trend did not reach statistical significance.

We also analyzed the density of distinct cell states in CR, non-CR, and untreated lesions and again observed increased densities of $CD8^+$ T cells and PD-1^-LAG-3^-TIM-3^- $CD8^+$ T cells, $CD4^+$ (helper) T cells, $CD4^+$ regulatory T cells, and B cells in CR lesions and increased densities of $CD25^+$ $CD4^+$ regulatory T cells in non-CR lesions, both compared with untreated lesions (Supplementary Fig. S9; Supplementary Table S8). We also observed an increase in the density of B cells and a decrease in the density of proliferating ($Ki67^+$) macrophages in CR lesions compared with untreated lesions (Supplementary Fig. S9; Supplementary Table S8).

Our examination of immune-cell states at the single-cell level suggested that effective antitumor immunity consequent to IL2 injection was characterized by the presence of nonproliferating T cells with a nonexhausted phenotype (PD-1^-LAG-3^-TIM-3^-). At the level of the transcriptome, we identified 70 genes that were differentially expressed in CR lesions compared with untreated lesions (**Fig. 2B**; Supplementary Table S9). This "IL2-response signature" included the upregulation of 25 genes associated with T-cell activation (e.g., *ADORA2A*, *CD69*, *DPP4*, *GZMM*, *STAT4*, and *TBX21*) and immune-cell localization to tumors (e.g., *CCL18*, *MARCO*, *CXCR6*, *GZMM*, *DPP4*, and *CD69*). Hierarchical clustering of the differentially expressed genes grouped untreated and non-CR lesions from the same patient, suggesting IL2 injection in the non-CR lesions failed to cause transcriptional reprogramming toward antitumor immunity. Interestingly, the clustering also grouped the four untreated lesions from the two patients who experienced complete regression of all injected lesions (extreme responders), indicating the presence of a transcriptional state that favors IL2 response.

One of the key goals of our analysis was to identify molecular or cellular changes in untreated lesions that might predict a complete lesion response to subsequent IL2 therapy. We therefore compared untreated lesions from "extreme responders" to the untreated lesions from patients for whom none or only some of the lesions had responded to IL2 (non-/mixed responders; **Fig. 3A**). Untreated lesions from extreme responders harbored a higher fraction of $CD8^+$ T cells and a lower fraction of $CD4^+$ T cells and MHC II^- macrophages (**Fig. 3B**; Supplementary Table S10). Untreated lesions from extreme responders also had higher fractions of proliferating T-cell populations, $CD27^+$ "activated" T- and NK-cell populations, B7-$H3^+$ macrophage populations and tumor cells, and PD-$L1^-$B7-$H3^-$IDO-1^- macrophage populations and tumor cells. Untreated lesions from extreme responders also harbored a higher fraction of PD-1^+LAG-3^+TIM-3^+ (exhausted) $CD8^+$ T cells and both exhausted and proliferating $CD8^+$ T cells, suggesting they were tumor reactive. We also observed a higher density of B cells in untreated lesions from extreme responders (Supplementary Fig. S10; Supplementary Table S11).

One of the most consistent differences between untreated lesions from extreme responders compared with non-/mixed responders was the higher fraction of $B2M^+$MHC I^+MHC II^- tumor cells (ID: 500) and lower fraction and lower density of $B2M^-$MHC I^-MHC II^- tumor cells (ID:506; **Fig. 3B**). In fact, there was near-complete overlap between the lack of MHC I and B2M expression on tumor cells and subsequent IL2 response failure at the single-cell level (**Fig. 3C**). We confirmed this finding by IHC staining for MHC I (**Fig. 3D**). All untreated lesions from extreme responders exhibited membranous MHC I positivity in at least 75% of tumor cells, whereas all untreated lesions from non-/mixed responders

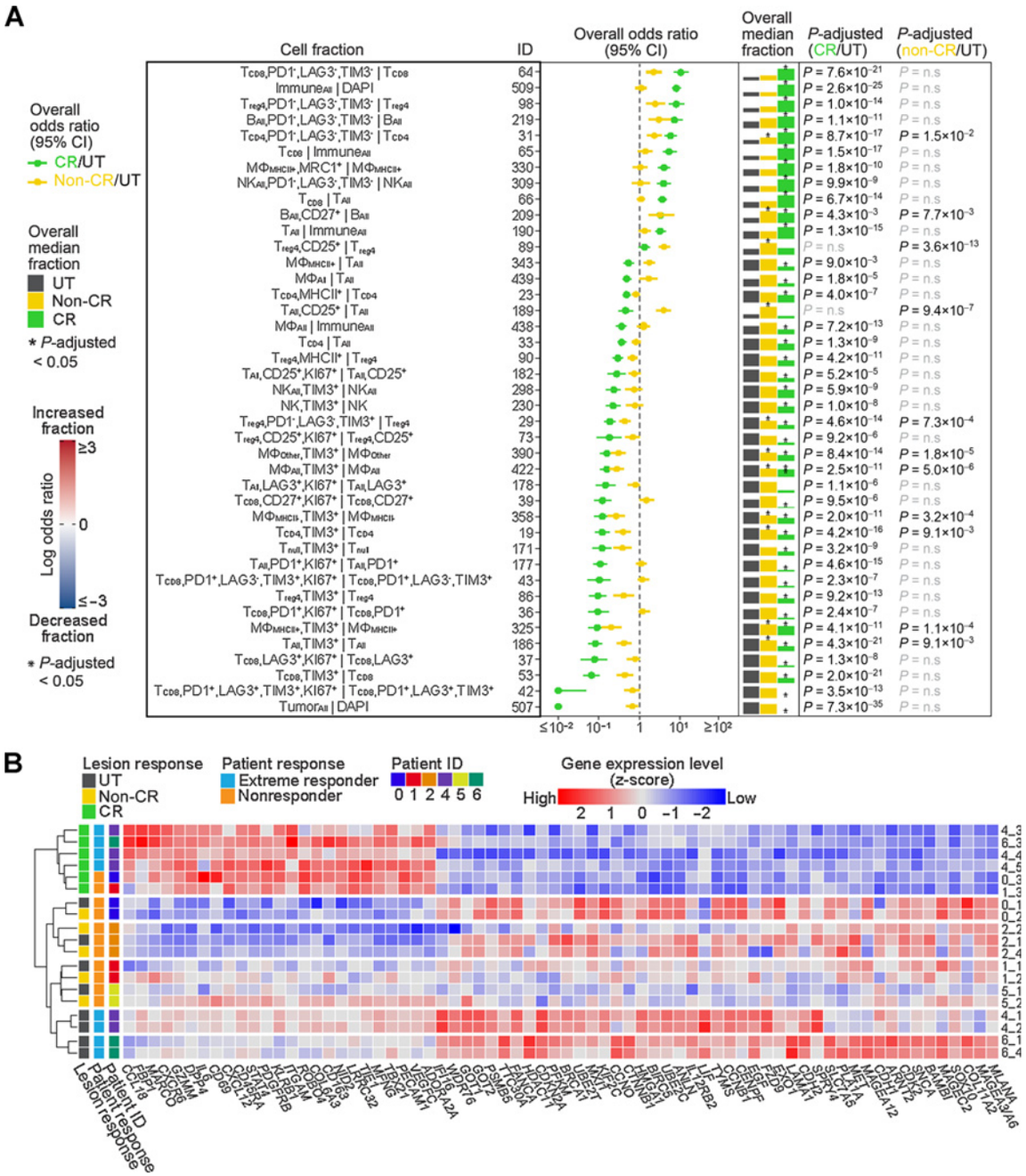

Figure 2.

Immune-cell states and gene-expression signatures following tumor-cell eradication by IL2. **A,** Shown are cell fractions (rows) with significant changes following IL2 injection. The forest plot shows the overall effect size (odds ratio) and 95% confidence interval (CI) of each cell fraction across all patients for CR ($n = 101$ FOV) versus untreated ($n = 112$ FOVs) and non-CR ($n = 120$ FOVs) versus untreated. The overall median fraction, scaled to 1 for the largest fraction, is shown for untreated, non-CR, and CR lesions. Significant results, determined using a two-sided Wilcoxon test adjusted by Bonferroni correction, are indicated with an asterisk above the median fraction with *P*-adjusted noted (n.s., not significant). See also Supplementary Table S6. See Supplementary Table S3 for full cell type names. **B,** The heatmap indicates scaled RNA expression values for differentially expressed genes (*P*-adjusted < 0.0001) in CR ($n = 6$) versus untreated ($n = 9$) and/or non-CR ($n = 5$) versus untreated, sorted by CR versus untreated fold change. See also Supplementary Table S9.

exhibited membranous MHC I positivity (if any) in fewer than 75% of tumor cells (**Fig. 3E**). We also found higher fractions of $B2M^{+}MHC\ I^{+}MHC\ II^{+}$ macrophage/monocytes in untreated lesions from extreme responders, suggesting MHC I expression in both tumor cells and macrophages is associated with IL2 response (Supplementary Fig. S11; Supplementary Table S10).

To confirm the association between tumor MHC I expression and CR to IL2, we performed IHC staining for MHC I in tumor biopsies

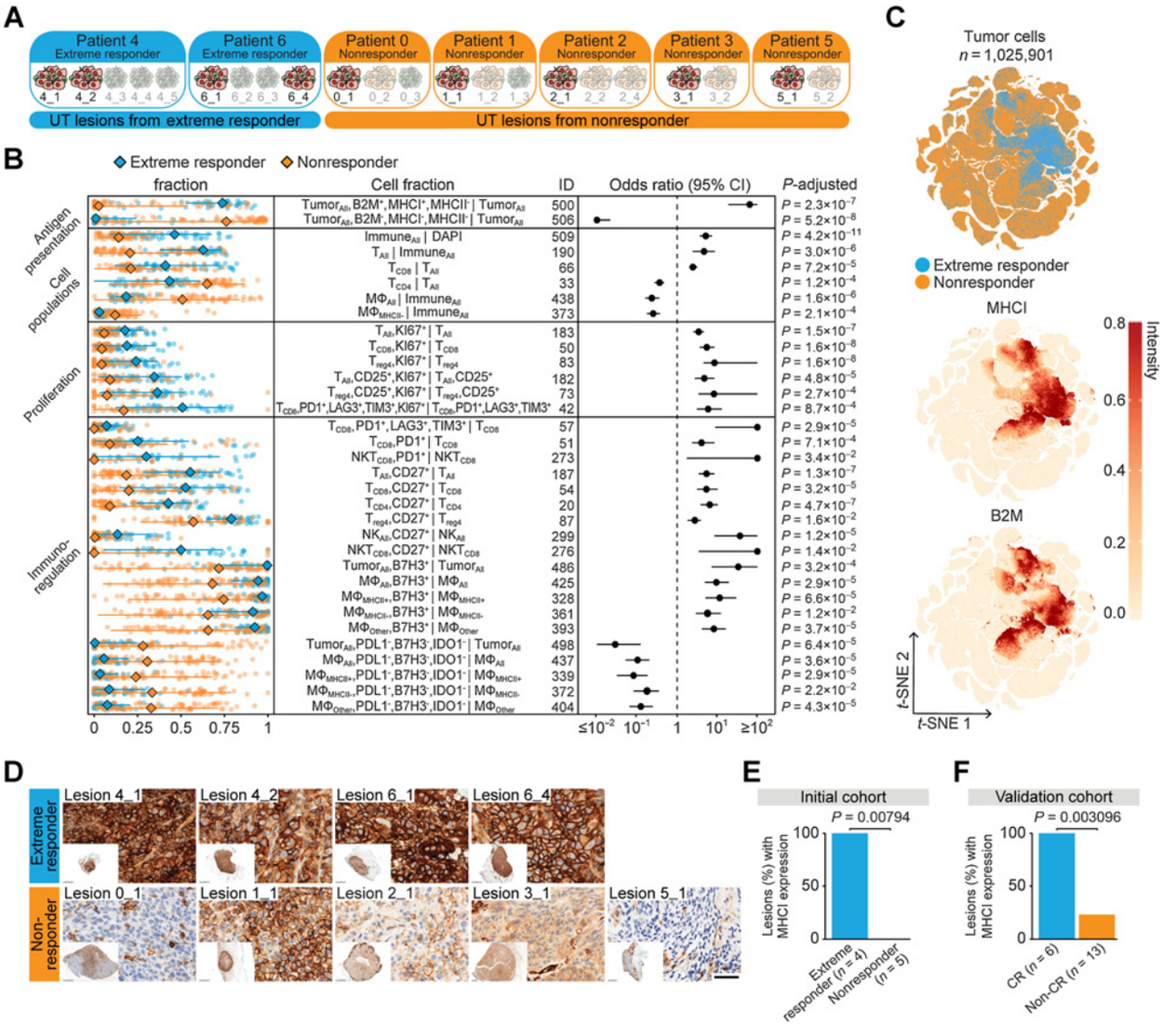

Figure 3.

Pretreatment tumor MHC I expression is associated with complete tumor response to IL2. **A,** Grouping of untreated (UT) lesions from extreme responder and non-/mixed responder patients (labeled "non-responder" throughout figures). **B,** Shown are cell fractions (rows) with significant differences in untreated lesions from extreme responders ($n = 38$ FOV) versus non-/mixed responders ($n = 74$ FOVs). Left, fractions in each FOV, with overall median, minimum, and maximum (each point represents an FOV). The forest plot shows effect size (odds ratio) and 95% CI of each cell fraction with *P*-adjusted noted (two-sided Wilcoxon test adjusted by Bonferroni correction). See also Supplementary Table S10. See Supplementary Table S3 for full cell type names. **C,** *t*-SNE of untreated lesion tumor cells colored by patient response and normalized intensity of MHC I and B2M. **D,** MHC I IHC of untreated lesions (scale bar, 50 μm). **E** and **F,** Bar graphs showing the percentage of untreated lesions with expression of membranous MHC I in greater than 75% of tumor cells in the initial cohort (**E**; extreme responder, $n = 4$; nonresponder, $n = 5$) and in the validation cohort (**F**; CR, complete responder, $n = 6$; non-CR, noncomplete responder, $n = 13$) based on IHC staining (Fisher exact test, two-sided, exact *P* value noted).

from 19 previously untreated patients with metastatic melanoma who subsequently received IL2 therapy (**Table 1**; Supplementary Table S12). We again found that all patients who had a CR exhibited membranous MHC I positivity in the vast majority (at least 75%) of tumor cells (**Fig. 3F**). Conversely, lack of membranous tumor MHC I expression was strongly associated with no or incomplete tumor response (non-CR; Supplementary Table S13).

Lack of membranous tumor MHC I expression was not associated with mutations in *B2M* or other antigen presentation–pathway related genes (Supplementary Fig. S12A). Untreated lesions from extreme responders showed significantly increased bulk RNA levels of *B2M*, *HLAB*, and *HLAC* (Supplementary Fig. S12B–S12F), consistent with our findings at the protein level. Loss of *B2M* RNA expression in bulk tumor was positively correlated with loss of MHC I protein expression on the tumor-cell membrane (Supplementary Fig. S12G).

Our data indicated that expression of MHC I protein on the tumor-cell membrane, which is required for antigen presentation, was associated with a higher fraction of exhausted and proliferating $CD8^+$ T cells. To explore this relationship in greater detail, we compared the functional state of immune cells in the immediate "neighborhood" (i.e.,

Table 1. Patient characteristics.

Cohort	Institution	Patient ID	Age	Gender	Lesion site	IL2 treatment	Patient response
Initial	MSKCC	4	42	M	Skin	Intralesional	CR
Initial	MSKCC	6	74	F	Skin	Intralesional	CR
Initial	MSKCC	0	56	M	Soft tissue	Intralesional	Non-CR
Initial	MSKCC	1	81	F	Skin	Intralesional	Non-CR
Initial	MSKCC	2	67	F	Soft tissue	Intralesional	Non-CR
Initial	MSKCC	3	86	F	Skin	Intralesional	Non-CR
Initial	MSKCC	5	69	M	Skin	Intralesional	Non-CR
Validation	Calgary	v_01	69	F	Skin	Intralesional	CR
Validation	Calgary	v_02	86	F	Skin	Intralesional	CR
Validation	Calgary	v_03	93	M	Skin	Intralesional	CR
Validation	NIH	v_04	52	M	Soft tissue	Systemic	CR
Validation	NIH	v_05	43	M	Skin	Systemic	CR
Validation	NIH	v_06	45	F	Lymph node	Systemic	CR
Validation	NIH	v_07	54	M	Skin	Systemic	Non-CR
Validation	NIH	v_08	63	F	Skin	Systemic	Non-CR
Validation	NIH	v_09	52	M	Soft tissue	Systemic	Non-CR
Validation	NIH	v_10	27	M	Lymph node	Systemic	Non-CR
Validation	NIH	v_11	48	M	Soft tissue	Systemic	Non-CR
Validation	NIH	v_12	48	M	Lung	Systemic	Non-CR
Validation	NIH	v_13	37	M	Lymph node	Systemic	Non-CR
Validation	MDACC	v_14	62	M	Lung	Systemic	Non-CR
Validation	MDACC	v_15	76	F	Skin	Systemic	Non-CR
Validation	MDACC	v_16	65	M	Lymph node	Systemic	Non-CR
Validation	MDACC	v_17	54	M	Lymph node	Systemic	Non-CR
Validation	JHMI	v_18	53	F	Skin	Systemic	Non-CR
Validation	JHMI	v_19	59	M	Skin	Systemic	Non-CR

Note: Clinical information for the metastatic melanoma patients in the initial cohort ($n = 7$) and in the validation cohort ($n = 19$) treated with either intralesional IL2 or high-dose systemic IL2. Patient response was classified as complete responder (CR; termed "extreme responder" in the initial cohort) or noncomplete responder (non-CR; termed "non-/mixed responder" in the initial cohort).

Abbreviations: Calgary, University of Calgary; JHMI, Johns Hopkins Medical Institute; MDACC, MD Anderson Cancer Center; MSKCC, Memorial Sloan Kettering Cancer Center; NIH, National Institutes of Health.

within 30 μm) of MHC I–high and MHC I–low tumor cells (Supplementary Fig. S13; Supplementary Table S14). MHC I–high neighborhoods harbored higher fractions of T cells and T-cell populations positive for CD27, PD-1, LAG-3, TIM-3, and MHC II, whereas MHC I–low neighborhoods harbored higher fractions of NK cells, consistent with the known inhibitory effect of MHC I on NK cells (14) and a dominant innate immune response in MHC I–low lesions.

We next examined the expression of immune-related genes in untreated lesions from extreme responders and non-/mixed responders where we found differential expression of 96 genes. Untreated lesions from extreme responders showed upregulation of several genes associated with IFNγ and IFNα signaling, antigen presentation, IL2 response, tertiary lymphoid structures (TLS), and T-cell dysfunction (**Fig. 4A**; Supplementary Table S15). Some of these gene-expression signatures (e.g., IFNγ signature and TLS) have been associated with clinical response to immune-checkpoint blockade (ICB) in melanoma (15, 16). We did not observe significant expression changes in genes that identify immune-cell populations, suggesting that upregulation of these gene-expression signatures in extreme responders was not simply a reflection of higher immune-cell counts (Supplementary Fig. S14). Given that tumor mutation burden (TMB) has been predictive of response to ICB (17), we determined TMB in our untreated lesions, but we found no instances of hypermutation (Supplementary Table S16).

One of the TLS-related and upregulated genes in untreated lesions from extreme responders was *CXCL13*, a B-cell attractant that is secreted by dysfunctional $CD8^+$ T cells (18, 19) and has been linked to clinical response to ICB (20). We therefore examined the spatial distribution of B cells and exhausted $CD8^+$ T cells relative to the tumor–stroma interface (±360 μm) in untreated lesions (**Fig. 4B**). We had previously observed increased densities of B cells in untreated lesions from extreme responders (Supplementary Fig. S10). Upon examining the spatial distribution of the B cells, we found that these B cells were predominantly in the stroma of extreme responders following intralesional IL2 (**Fig. 4C**; Supplementary Table S17). Although our review of H&E stains of the untreated lesions did not identify TLS, using multiplexed IF we observed a greater number of $CD20^+$ B-cell aggregates, which were surrounded by both $CD8^+$ and $CD4^+$ T cells, in untreated lesions from extreme responders (**Fig. 4D–F**; Supplementary Table S17).

Next, we examined the degree of $CD8^+$ T-cell exhaustion (**Fig. 4G**) as a function of their spatial distribution relative to the tumor–stroma interface (**Fig. 4H**; Supplementary Table S18). In untreated lesions, we observed increasing fractions of PD-1^+LAG-3^+TIM-3^+ exhausted $CD8^+$ T cells, as $CD8^+$ T cells approach the tumor interface from both the stroma (–360 μm) and from within the tumor (+360 μm; Supplementary Fig. S15A and S15B; Supplementary Table S18). We observed increased densities of several $CD8^+$ T-cell populations (i.e., expressing different combinations of PD-1, LAG-3, and TIM-3) in both the tumor (–360:0 μm) and stroma regions (0:360 μm) of extreme responders compared with non-/mixed responders (**Fig. 4I**; Supplementary Table S18).

To identify potential contributors of $CD8^+$ T-cell exhaustion, we also characterized the cellular neighborhood of $CD8^+$ T cells as they progress from a TN (PD-1^-LAG-3^-TIM-3^-) to TP (PD-1^+LAG-3^+TIM-3^+) state (**Fig. 4J**; Supplementary Table S19). As $CD8^+$ T cells

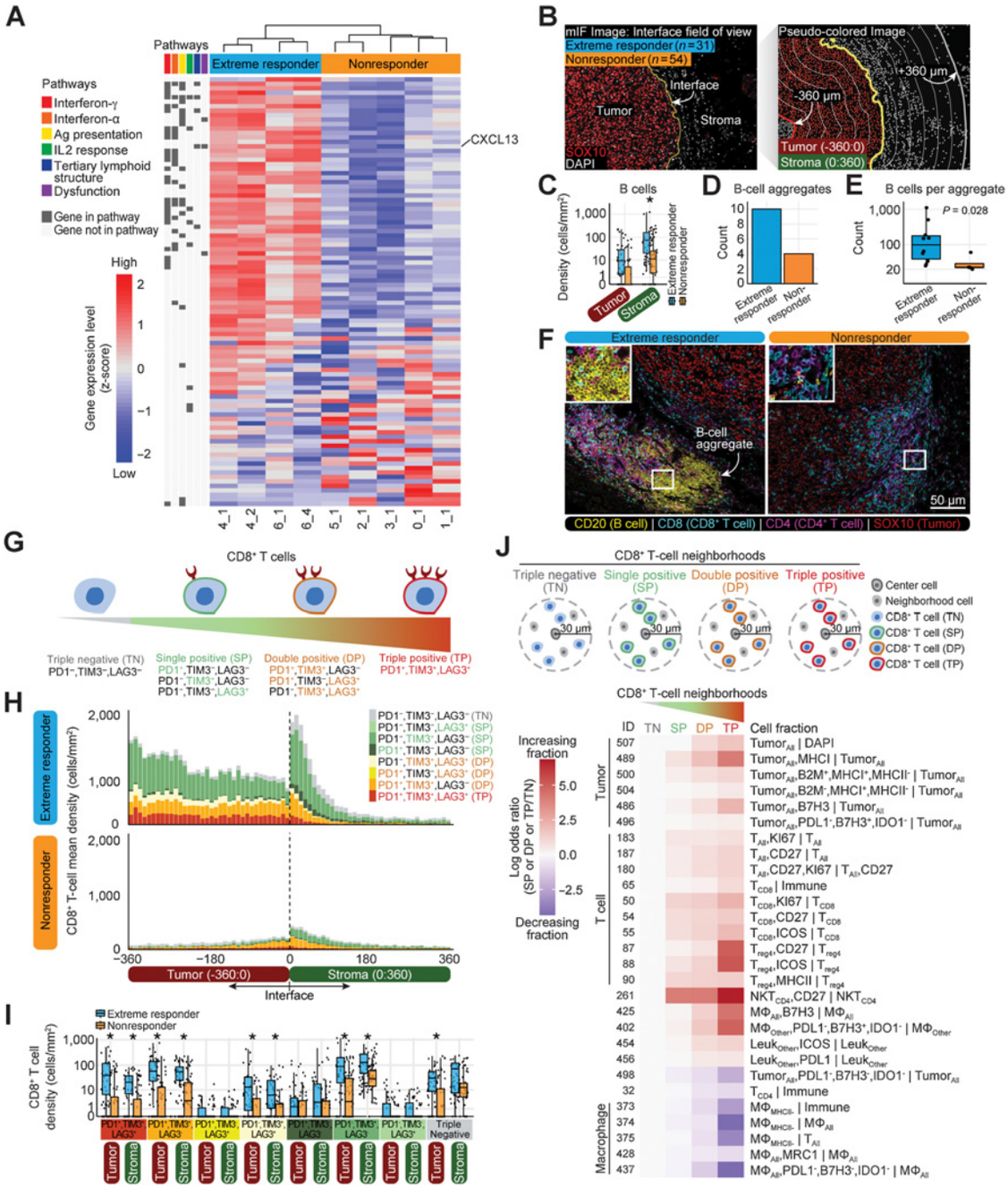

Figure 4.

Activated tumor microenvironment prior to IL2 treatment characterizes extreme responders. **A,** The heatmap indicates scaled RNA expression values for differentially expressed genes (*P*-adjusted < 0.05) in untreated lesions from extreme responders ($n = 4$) versus non-/mixed responders (labeled "non-responder" throughout figures; $n = 5$), sorted by fold change. See also Supplementary Table S15. **B,** Schematic of tumor interface analysis. mIF, multiplexed IF. **C,** Box plots showing B-cell density in tumor and stroma of untreated lesions (minimum, median, and maximum with each point representing an FOV). Significant results, determined using a two-sided Wilcoxon test adjusted by Bonferroni correction, are indicated with an asterisk (*P*-adjusted<0.05). See also Supplementary Table S17. **D,** Total B-cell aggregate counts in untreated lesions. **E,** Total count of B cells per aggregate (Wilcoxon rank sum test, exact *P* value noted) in untreated lesions [extreme responder ($n = 10$) and nonresponder ($n = 4$)]. **F,** Representative multiplexed IF images from an untreated lesion of an extreme responder (6_4) and non-/mixed responder (1_1) showing B-cell aggregates. **G,** Cartoon of $CD8^+$ T-cell states. **H,** Mean density of $CD8^+$ T cells expressing all combinations of PD-1/TIM-3/LAG-3 in untreated lesions in 10-µm intervals from −360:360 µm. See also Supplementary Table S18. **I,** Box plots showing density of $CD8^+$ T cells expressing all combinations of PD-1/TIM-3/LAG-3 in tumor and stroma of untreated lesions (minimum, median, and maximum with each point representing an FOV). See also Supplementary Table S18. **J,** $CD8^+$ T-cell neighborhood definitions. The heatmap indicates effect size (odds ratio) of each cell fraction (rows) in untreated lesions for SP/DP/TP neighborhoods normalized against TN neighborhoods. See also Supplementary Table S19.

become exhausted (PD-1$^+$LAG-3$^+$TIM-3$^+$), their neighborhood is characterized by increasing fractions of B2M$^+$MHC I$^+$MHC II$^-$ tumor cells, proliferating/activated (Ki67$^+$, CD27$^+$, or ICOS$^+$) T and NK cells, B7-H3$^+$ macrophages and tumor cells, and decreasing fractions of CD4$^+$ T cells, MHC II$^-$ macrophages, and PD-L1$^-$B7-H3$^-$IDO-1$^-$ macrophage and tumor cells in their cellular neighborhoods.

Discussion

Clinical response to ICB has been extensively studied and associated with both tumor cell–intrinsic factors (including TMB, HLA expression, and PD-L1 expression; refs. 17, 21) and tumor microenvironment factors (including TLS and dysfunctional T cells; refs. 16, 18, 22). There are presently no known biomarkers of response for IL2. Our data show that the absence of membranous MHC I in tumor cells is associated with the failure to respond to IL2. This finding emerged from our multidimensional analysis of in-transit metastases from seven melanoma patients receiving intralesional IL2 and was subsequently confirmed in an independent multi-institutional validation cohort of 19 patients with metastatic melanoma. Of note, melanoma patients in our validation cohort had received IL2 therapy in either an intralesional or high-dose systemic formulation, broadening the impact of this biomarker to melanoma patients receiving systemic IL2. Expression of MHC I on the tumor-cell membrane in melanoma has also been reported to be associated with clinical response to anti–CTLA-4, but not anti–PD-1 ICB (23).

In addition to widespread tumor-cell MHC I expression, untreated lesions from "extreme responders" showed hallmarks of a tumor-reactive microenvironment, with stromal B-cell aggregates, increased expression of IFNγ, IFNα, and IL2 response–related genes, and CD8$^+$ T cells with an "exhausted" phenotype. The immune-cell infiltrate after complete eradication of all tumor cells, on the other hand, was characterized by CD8$^+$ T cells with a "non-exhausted" phenotype. Given the limitations of our study design, we were unable to determine the molecular basis of this "switch" in CD8$^+$ T-cell phenotype. It might represent an IL2-induced reversal of a preexistent exhausted state, novel trafficking of naïve CD8$^+$ T cells into these lesions, local expansion of naïve CD8$^+$ T cells in these lesions, or a combination thereof (24–26). Further studies with sequential tumor biopsies may be able to address this important mechanistic question.

Our study combined *in situ* single-cell profiling with bulk RNA and DNA profiling from adjacent unstained tissue sections of FFPE tumor, a biospecimen source that is widely available for the majority of cancer patients. This approach allowed us to identify therapy-associated cell states and gene-expression signatures and generate immunotherapy response biomarker hypotheses. Because the single-cell data architecture, spatial analytics, and biostatistical outputs developed in our work are platform agnostic and expandable to any number of cell phenotypes, our approach could be helpful to guide the clinical development of other immunotherapies for cancer.

Authors' Disclosures

D.S. Klimstra reports personal fees from Paige.AI outside the submitted work. E.J. Lipson reports personal fees from Bristol Myers Squibb, Novartis, EMD Serono, Array BioPharma, Macrogenics, Merck, Sanofi/Regeneron, Genentech, Odonate Therapeutics, Eisai, and Natera outside the submitted work. J.M. Taube reports grants and other support from Bristol Myers Squibb, Merck, and AstraZeneca, and grants, nonfinancial support, and other support from Akoya Biosciences outside the submitted work, as well as a patent for multiplex IHC pending. J.A. Wargo reports other support from Micronoma and PeerView outside the submitted work. M.K. Callahan reports grants from Bristol Myers Squibb and personal fees from Merck, AstraZeneca, ImmunoCore, and Moderna outside the submitted work. I.K. Mellinghoff reports grants from NINDS, Geoffrey Beene Cancer Research Center, and Cycle for Survival and a Cancer Center Support Grant during the conduct of the study; personal fees from Roche, Prelude Therapeutics, Black Diamond Therapeutics, Agios, Debiopharm Group, Erasca, and Puma Biotechnology, nonfinancial support and other support from Servier Pharmaceuticals and Voyager Therapeutics, and other support from DC Europa Ltd., Kazia Therapeutics, Novartis, Cardinal Health, Samus Therapeutics, Vigeo Therapeutics, Amgen, General Electric, Lilly, AstraZeneca, and GCAR outside the submitted work; and a patent with the patent application number 63/293,986 (related to the the submitted work) pending. T.J. Hollmann reports other support from Parker Institute for Cancer Immunotherapy, and grants from Bristol Myers Squibb and Calico Labs during the conduct of the study. No disclosures were reported by the other authors.

Authors' Contributions

M. Pourmaleki: Conceptualization, resources, data curation, software, formal analysis, supervision, investigation, visualization, methodology, writing–original draft, writing–review and editing. **C.J. Jones:** Software, formal analysis, visualization, methodology, writing–review and editing. **C.E. Ariyan:** Resources, writing–review and editing. **Z. Zeng:** Software, formal analysis, writing–review and editing. **M. Pirun:** Software, formal analysis, writing–review and editing. **D.A. Navarrete:** Formal analysis, writing–review and editing. **Y. Li:** Formal analysis, writing–review and editing. **M. Zhang:** Formal analysis, writing–review and editing. **S. Nandakumar:** Data curation, formal analysis, writing–review and editing. **C. Campos:** Resources, formal analysis, supervision, writing–review and editing. **S. Nadeem:** Resources, writing–review and editing. **D.S. Klimstra:** Resources, writing–review and editing. **C.F. Temple-Oberle:** Validation, writing–review and editing. **T. Brenn:** Validation, writing–review and editing. **E.J. Lipson:** Validation, writing–review and editing. **K.M. Schenk:** Validation, writing–review and editing. **J.E. Stein:** Validation, writing–review and editing. **J.M. Taube:** Validation, writing–review and editing. **M.G. White:** Validation, writing–review and editing. **R. Traweek:** Validation, writing–review and editing. **J.A. Wargo:** Validation, writing–review and editing. **J.M. Kirkwood:** Validation, writing–review and editing. **B. Gasmi:** Validation, writing–review and editing. **S.L. Goff:** Validation, writing–review and editing. **A.D. Corwin:** Software, writing–review and editing. **E. McDonough:** Software, writing–review and editing. **F. Ginty:** Software, writing–review and editing. **M.K. Callahan:** Validation, writing–review and editing. **A. Schietinger:** Supervision, investigation, methodology, writing–review and editing. **N.D. Socci:** Data curation, software, formal analysis, visualization, methodology, writing–review and editing. **I.K. Mellinghoff:** Conceptualization, resources, supervision, writing–original draft, writing–review and editing. **T.J. Hollmann:** Conceptualization, resources, supervision, writing–original draft, writing–review and editing.

Acknowledgments

We thank Hedvig Hricak, Anup Sood, Jedd Wolchok, and members of the Mellinghoff, Hollmann, and Socci research groups for their helpful suggestions and support with this project. We thank Steven A. Rosenberg and James C. Yang (NCI, NIH), Russell Witt (The University of Texas MD Anderson Cancer Center), and Elizabeth Rush and Cindy Sander (University of Pittsburgh) for their help with obtaining patients for the validation cohort. We acknowledge the use of the Integrated Genomics Operation Core, funded by an NCI Cancer Center Support Grant (CCSG; P30 CA08748), Cycle for Survival, and the Marie-Josée and Henry R. Kravis Center for Molecular Oncology. This study was financially supported by NIH grant 1 R35 NS105109 03 (I.K. Mellinghoff), NIH grant T32 GM132083 (M. Pourmaleki), NIH grant P30CA008748 (MSK Cancer Center Support Grant), the Geoffrey Beene Cancer Research Center (I.K. Mellinghoff), Cycle for Survival (I.K. Mellinghoff), Parker Institute for Cancer Immunotherapy (C.E. Ariyan, Y. Li, and T.J. Hollmann), NIH grant 1 R01 CA219896-01A1 (J.A. Wargo), Melanoma Research Alliance (J.A. Wargo), SU2C-AACR-IRG-19-17 (J.A. Wargo), MD Anderson Cancer Center's Melanoma Moon Shots Program (J.A. Wargo), NIH grant T32 CA 009599 (M.G. White), MD Anderson Cancer Support grant P30 CA016672 (M.G. White), P50 CA254865-01A1 (J.M. Kirkwood), Melanoma and Skin Cancer SPORE (J.M. Kirkwood), and NCI Center for Cancer Research (S.L. Goff).

The costs of publication of this article were defrayed in part by the payment of page charges. This article must therefore be hereby marked *advertisement* in accordance with 18 U.S.C. Section 1734 solely to indicate this fact.

Received December 17, 2021; revised January 3, 2022; accepted January 4, 2022; published first January 10, 2022.

References

1. Meier F, Will S, Ellwanger U, Schlagenhauff B, Schittek B, Rassner G, et al. Metastatic pathways and time courses in the orderly progression of cutaneous melanoma. Br J Dermatol 2002;147:62–70.
2. Coit DG, Thompson JA, Algazi A, Andtbacka R, Bichakjian CK, Carson WE, et al. Melanoma, version 2.2016, NCCN clinical practice guidelines in oncology. J Natl Compr Cancer Netw 2016;14:450–73.
3. Byers BA, Temple-Oberle CF, Hurdle V, McKinnon JG. Treatment of in-transit melanoma with intra-lesional interleukin-2: a systematic review. J Surg Oncol 2014;110:770–5.
4. Mullard A. Restoring IL-2 to its cancer immunotherapy glory. Nat Rev Drug Discov 2021;20:163–5.
5. Read T, Lonne M, Sparks DS, David M, Wagels M, Schaider H, et al. A systematic review and meta-analysis of locoregional treatments for in-transit melanoma. J Surg Oncol 2019;119:887–96.
6. Radny P, Caroli UM, Bauer J, Paul T, Schlegel C, Eigentler TK, et al. Phase II trial of intralesional therapy with interleukin-2 in soft-tissue melanoma metastases. Br J Cancer 2003;89:1620–6.
7. Hassan S, Petrella TM, Zhang T, Kamel-Reid S, Nordio F, Baccarelli A, et al. Pathologic complete response to intralesional interleukin-2 therapy associated with improved survival in melanoma patients with in-transit disease. Ann Surg Oncol 2015;22:1950–8.
8. Zehir A, Benayed R, Shah RH, Syed A, Middha S, Kim HR, et al. Mutational landscape of metastatic cancer revealed from prospective clinical sequencing of 10,000 patients. Nat Med 2017;23:703–13.
9. Gerdes MJ, Sevinsky CJ, Sood A, Adak S, Bello MO, Bordwell A, et al. Highly multiplexed single-cell analysis of formalin-fixed, paraffin-embedded cancer tissue. Proc Natl Acad Sci U S A 2013;110:11982–7.
10. Sood A, Miller AM, Brogi E, Sui Y, Armenia J, McDonough E, et al. Multiplexed immunofluorescence delineates proteomic cancer cell states associated with metabolism. JCI Insight 2016;1:87030.
11. Acharya N, Sabatos-Peyton C, Anderson AC. Tim-3 finds its place in the cancer immunotherapy landscape. J Immunother Cancer 2020;8:e000911.
12. Wolf Y, Anderson AC, Kuchroo VK. TIM3 comes of age as an inhibitory receptor. Nat Rev Immunol 2020;20:173–85.
13. Cesana G, Iodice G, Cohen S, Moroziewicz D, Mitcham J, Stoutenburg J, et al. Characterization of CD4+CD25+ regulatory T cells in patients treated with high-dose interleukin-2 for metastatic melanoma or renal cell carcinoma. J Clin Oncol 2006;24:1169–77.
14. Raulet DH, Gasser S, Gowen BG, Deng W, Jung H. Regulation of ligands for the NKG2D activating receptor. Annu Rev Immunol 2013;31:413–41.
15. Grasso CS, Tsoi J, Onyshchenko M, Abril-Rodriguez G, Ross-Macdonald P, Wind-Rotolo M, et al. Conserved interferon-γ signaling drives clinical response to immune checkpoint blockade therapy in melanoma. Cancer Cell 2020;38:500–15.
16. Cabrita R, Lauss M, Sanna A, Donia M, Skaarup Larsen M, Mitra S, et al. Tertiary lymphoid structures improve immunotherapy and survival in melanoma. Nature 2020;577:561–5.
17. Yarchoan M, Albacker LA, Hopkins AC, Montesion M, Murugesan K, Vithayathil TT, et al. PD-L1 expression and tumor mutational burden are independent biomarkers in most cancers. JCI Insight 2019;4:e126908.
18. van der Leun AM, Thommen DS, Schumacher TN. CD8+ T cell states in human cancer: insights from single-cell analysis. Nat Rev Cancer 2020;20:218–32.
19. Li H, van der Leun AM, Yofe I, Lubling Y, Gelbard-Solodkin D, van Akkooi ACJ, et al. Dysfunctional CD8 T cells form a proliferative, dynamically regulated compartment within human melanoma. Cell 2019;176:775–89.
20. Litchfield K, Reading JL, Puttick C, Thakkar K, Abbosh C, Bentham R, et al. Meta-analysis of tumor- and T cell-intrinsic mechanisms of sensitization to checkpoint inhibition. Cell 2021;184:596–614.
21. Chowell D, Morris LGT, Grigg CM, Weber JK, Samstein RM, Makarov V, et al. Patient HLA class I genotype influences cancer response to checkpoint blockade immunotherapy. Science 2018;359:582–7.
22. Miller BC, Sen DR, Al Abosy R, Bi K, Virkud YV, LaFleur MW, et al. Subsets of exhausted CD8 + T cells differentially mediate tumor control and respond to checkpoint blockade. Nat Immunol 2019;20:326–36.
23. Rodig SJ, Gusenleitner D, Jackson DG, Gjini E, Giobbie-Hurder A, Jin C, et al. MHC proteins confer differential sensitivity to CTLA-4 and PD-1 blockade in untreated metastatic melanoma. Sci Transl Med 2018;10:eaar3342.
24. Spolski R, Li P, Leonard WJ. Biology and regulation of IL-2: from molecular mechanisms to human therapy. Nat Rev Immunol 2018;18:648–59.
25. Boyman O, Sprent J. The role of interleukin-2 during homeostasis and activation of the immune system. Nat Rev Immunol 2012;12:180–90.
26. Kalia V, Sarkar S. Regulation of effector and memory CD8 T cell differentiation by IL-2—a balancing act. Front Immunol 2018;9:2987.